Chapter 5

Single-Stage Integration of PMSG Based WECS in DC Microgrid

5.1 Introduction

The free availability of alternative sources of energy can significantly improve living standards in areas deprived of conventional energy sources [113]. Hydel power has the maximum share among the available installed capacity of renewable sources. However, with the unavailability of appropriate topological sites and high installation cost, it is not experiencing much growth in the last two decades. Solar and wind power are the fastest growing alternative energy sources because of economic affordability and advancement in power electronics and control [88, 114].

Extensive studies have been done on the adverse effect of renewable energy integration into the power grid [17, 79, 114, 115]. Although these shortcomings can be overcome by advanced control strategy [90, 116] and converter modification [8, 17, 87, 88, 94]. A more viable solution to this problem is integrating renewable sources into the DC microgrids [12, 117]. The majority of the household loads are effectively DC in nature, and [32] states that the end-to-end efficiency with a DC microgrid is higher than an AC microgrid with DC loads. An economically suitable and efficient DC converter is required for maximum power point tracking (MPPT) and energy flow control to integrate the renewable sources into a DC microgrid.

The grid-connected WECS are based on partial scale power in the case of doubly fed induction generator (DFIG) and full-scale converters in the case of PMSG and SEIG [118].

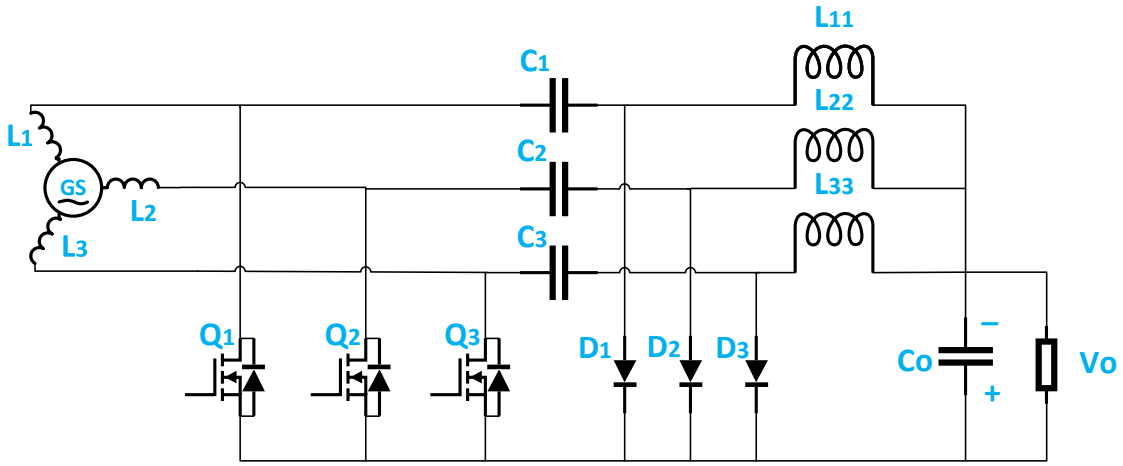

Figure 5.1: Topology of the bridgeless ĉuk converter.

This was the main reason for the popularity of DFIG for wind energy conversion systems (WECS). Still, with increasing power levels of wind turbines, the partial converter rating is redundant as many power converters in parallel are used for grid integration. Full-scale converters are more versatile as they can be used for active stall techniques in high wind speed conditions [84]. Thus, PMSG with a full-scale converter is more suitable for low-power standalone DC microgrid applications. Moreover as PMSG with a high voltage constant can operate at low wind speeds without a gearbox. The elimination of gearbox, brush contact, and rotor losses in PMSG driven WECS increase system reliability and lower overall cost [116, 119]. PMSG is considered more relevant for rural applications in this work due to its robustness and low maintenance.

The proposed three-phase AC-DC bridgeless ĉuk converter is shown in Figure 5.1. It has a fewer number of switches, has simple control, and can operate in a broader voltage range. It is designed and developed to be tested with PMSG driven by a squirrel cage induction motor (SCIM) based wind turbine emulator. The motivation of this work is to implement this converter in WECS for rural and isolated areas. The chapter is organized as follows: converter circuit description, operation, and small-signal analysis are briefed in section II. Section III deals with the description of the WECS setup used in this work and converter design. The simulation results with brief discussions are collated in section IV. Section V presents the hardware results. The conclusion is drawn in section VI.

5.2 Bridgeless Ĉuk Converter

5.2.1 Circuit description

Figure 5.1 illustrates the three-phase AC-DC converter. The proposed converter can operate with a three-phase generator with phase inductances of L_1, L_2, & L_3, followed by a modified bridgeless ĉuk converter topology. The switches Q_1, Q_2, & Q_3 are used for energising the phase inductors. Capacitors C_1, C_2, & C_3 are then charged on turn 'OFF' of switches through the diodes D_1, D_2, & D_3 respectively. The capacitors discharge the stored energy in the output capacitor C_o through the output inductors L_{11}, L_{22}, & L_{33}. Over the conventional bridgeless ĉuk converter the proposed topology has following advantages:

1. There are no diodes connected directly to the source; thus, stator inductance of generator can be used as the input inductance.

2. The switching control is simple and thus needs fewer components as a single gate driver can be used to switch all three switches.

3. Three-phase bridgeless ĉuk converter topology ensures only 50 percent working cycle for capacitors, output inductors, and diodes.

4. The back diodes of the switches are used in the negative half cycle of the source voltage in the respective phases, which leads to further component reduction.

5.2.2 Converter operation

The converter is designed to operate in continuous inductor current mode (CICM) at the input inductances. While the output inductors are working in discontinuous inductor current mode (DICM). This ensures inherent PFC and allows the converter to operate more efficiently by drawing only the active power from the generator. The operation of the converter is defined in the following three modes.

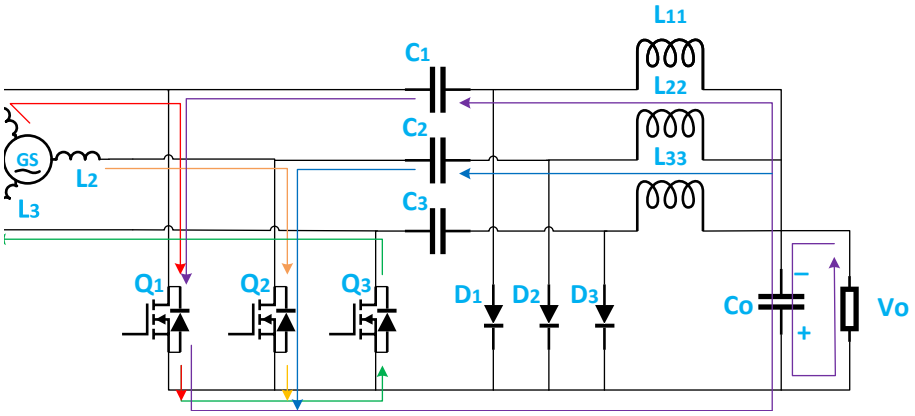

Figure 5.2: Mode-1 of converter operation.

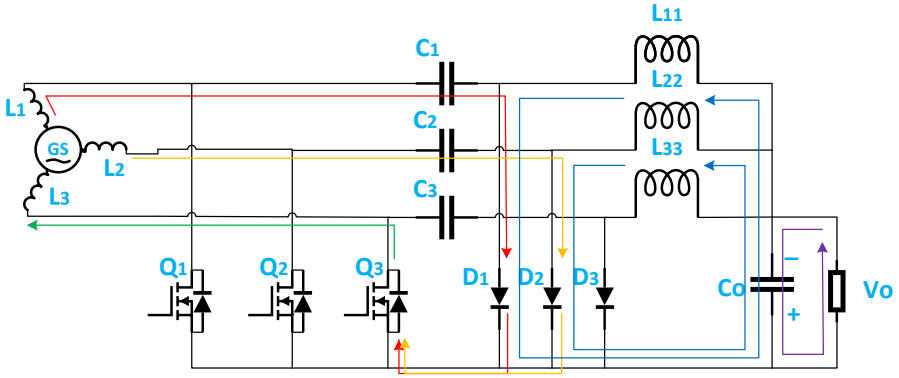

Figure 5.3: Mode-2 of converter operation.

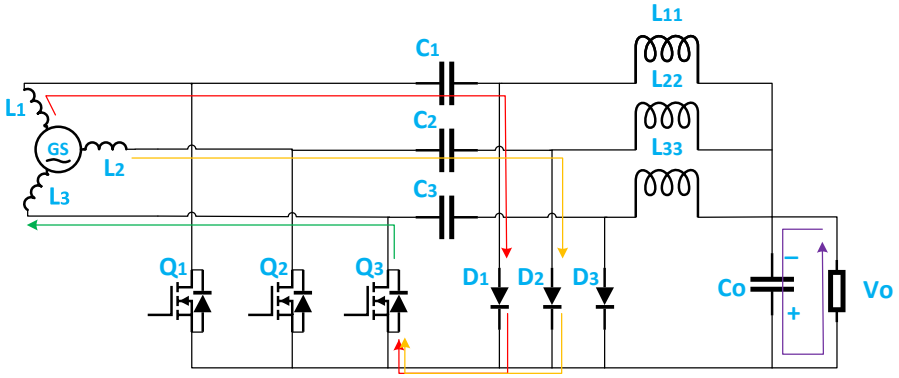

Figure 5.4: Mode-3 of converter operation.

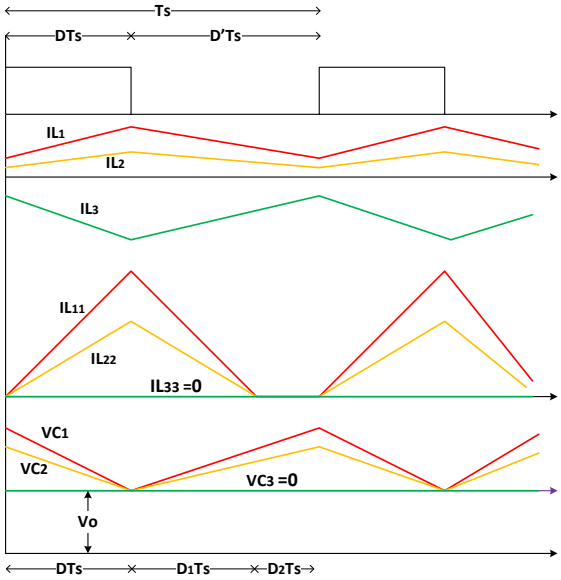

Figure 5.5: Key waveforms of converter operation.

Mode-1

In mode-1 of converter operation is depicted in Figure 5.2, switches Q_1-Q_3 are switched 'ON' simultaneously, which allows the input inductors to be charged in a positive or negative direction depending on the voltage of the respective phases. In Figure 5.2 the R & Y phases have positive voltage, and phase B has a negative voltage. As the output inductors are in the discontinuous inductor current mode (DICM), all the output inductors are fully discharged at the start of this mode. The currents in output inductors start from zero as they are charged by the intermediate capacitors $C_1 - C_3$.

Mode-2

Figure 5.3 depicts Mode-2 of the converter operation. In this mode, all the switches are turned 'OFF,' and the input inductors ($L_1 - L_3$) are discharging their energy in capacitors ($C_1 - C_3$) through diodes ($D_1 - D_3$). In this mode, the input inductors in the phases with positive voltage (R and Y) are discharging their energy in capacitors (C_1 & C_2). The inductor in the negative phase (B) is also discharging its energy in the same capacitors through the back diode of the switch (Q_3). In this mode, the output inductors (L_{11} and L_{22}) are discharging in the output capacitor through diodes (D_1 and D_2).This mode ends when output inductors are fully discharged.

Mode-3

The mode-3 of converter operation is depicted in Figure 5.4. In this mode, the switches continue to be in the 'OFF' state. All the output inductors are fully discharged. The input inductors continue to discharge in the intermediate capacitor through diodes (D_1 and D_2) as these inductors are operating in CICM.

The keywaveforms of the input current, output inductor current and the capacitor voltage is shown in Figure 5.5.

5.2.3 Small signal analysis

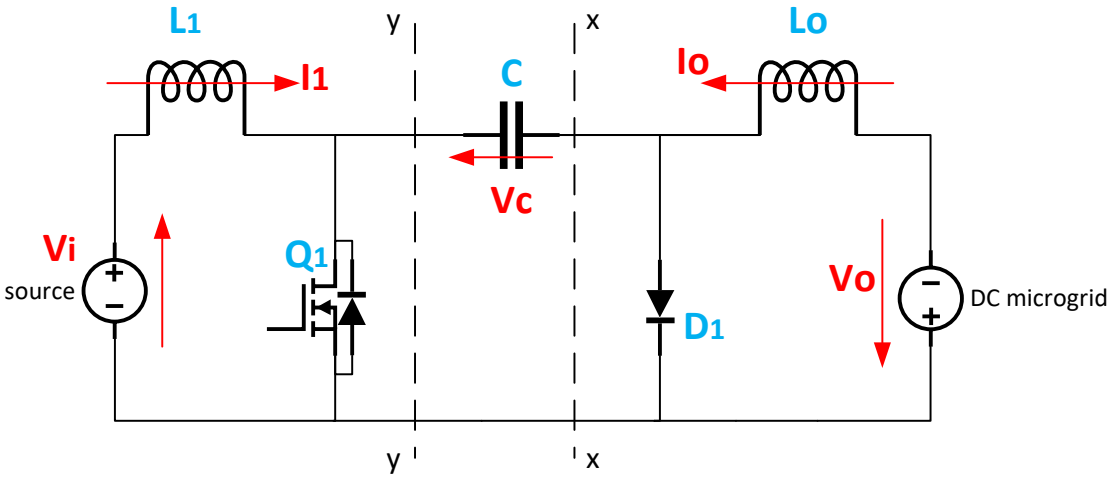

Figure 5.6: Equivalent circuit for small signal analysis.

The converter is analyzed using the current injected equivalent circuit method [120]. A single-phase model of the converter is used for analysis and small-signal transfer function. In Figure 5.6, the circuit is divided into two parts for analysis. The circuit from input to xx is the input part, while part of the circuit from yy to the output is the output ports of the converter. For the first part of the circuit, V_c is the output, and the input is the V_in. 'D_1' represents the 'ON' time of the switch, and 'D_2' represents the 'OFF' time. The average inductor current injected in capacitor C is given by:

$$i_{avg} = D_2.I_1 \tag{5.1}$$

Derivative of the input inductor current is given by:

$$\frac{L_1 dI_1}{dt} = V_{in} - D_2.V_c \tag{5.2}$$

Let the effective load on the capacitor 'C' is 'R_e', then

$$V_c = i_{avg}.(C \parallel R_e) \tag{5.3}$$

Where,

$$R_e = V_o/I_o \tag{5.4}$$

from the output part of the circuit, the derivative of inductor current is given by:

$$\frac{L_o dI_o}{dt} = D_1.V_c - V_o \tag{5.5}$$

Perturbing (1)-(4) around the steady state and taking the laplace transform, the small signal linear equations are found as,

$$\hat{i}_{avg} = D_2.\hat{i}_1 - I_1.\hat{d}_1 \tag{5.6}$$

$$sL_1\hat{i}_1 = \hat{V}_{in} - D_2.\hat{V}_c + V_c.\hat{d}_1 \tag{5.7}$$

$$\hat{v}_c = R.\hat{i}_{avg} - \frac{I_1.D_2.R.\hat{i}_o}{I_o} \tag{5.8}$$

Where,

$$R = \frac{V_o}{sCV_o + I_o}$$

Solving (6)-(8) yields,

$$\hat{V}_c\left(\frac{1}{R} + \frac{D_2^2}{sL_1}\right) = \frac{D_2}{sL_1}\hat{v}_{in} + \frac{V_o.D_2}{sL_1.D_1}\hat{d}_1 - \frac{1}{D_1}\hat{i}_o \tag{5.9}$$

In output part of the converter, the state of the output capacitor is not perturbed as the converter is employed in a DC microgrid of 230 V. The stiff DC voltage on the output makes it a constant quantity. Thus, (5) is perturbed to get the following equation,

$$sL_2\hat{i}_o = D_1.\hat{v}_c + V_c.\hat{d}_1 \tag{5.10}$$

Thus, solving (9) & (10) yields the following,

$$\left[sL_2 + \frac{1}{X}\right]\hat{i}_o = \frac{D_1.D_2}{sX.L_1}\hat{v}_{in} + \left(\frac{V_o.D_2}{sX.L_1} + \frac{V_o}{D_1}\right)\hat{d}_1 \tag{5.11}$$

Where,

$$X = \frac{1}{R} + \frac{D_2^2}{sL_1} \tag{5.12}$$

As the output power is proportional to the output current(I_o), the control to output current transfer function is presented here by putting $\hat{v}_{in}$=0 in (11).

$$\frac{\hat{i}_o}{\hat{d}_1} = \frac{s^2 L_1^2 V_o^2 C + s L_1^2 V_o I_o + L_1 V_o^2 D_2}{s^3 L_1^2 D_1 L_2 V_o C + s^2 L_1^2 I_o D_1 L_2 + s L_1 L_2 D_1 D_2^2 V_o + L_1 D_1} \tag{5.13}$$

5.3 WECS Description and Converter Design

In order to test the proposed converter, a WECS is realized. It consists of a wind turbine emulator, a proposed converter, and a DC load. The emulator is developed using a SCIM driven by using decoupled Field-Oriented Control (FOC). In this work, a MOD-2 turbine type is emulated as it has a simpler mathematical model and has a higher value of Tip-speed Ratio (TSR). Higher TSR(λ) value is more apt for the direct-drive PMSG based WECS, as higher rotor speed is achieved at all wind speeds. The parameters of the PMSG used in this work are given in Table 5.1.

5.3.1 MOD-2 turbine model

The power coefficient (C_p), which depends on TSR(λ) and blade pitch (β), decides the amount of energy extracted from the wind by the turbine. For a blade of radius 'r', cross-sectional area 'A', rotating with an angular velocity of 'ω_r' in a wind of speed 'V_w', the value of TSR(λ), 'C_p' and wind turbine power is given as:

$$\lambda = \frac{\text{Tip Speed of Blade}}{\text{Wind Speed}} = \frac{\omega_r . r}{V_w} \tag{5.14}$$

$$C_p = C_1(C_2 - C_3\beta - C_4\beta^x - C_5)e^{-C_6(\lambda,\beta)} \tag{5.15}$$

$$P_{turbine} = \frac{1}{2} C_p \rho A v^3 \tag{5.16}$$

Using (5.15) and [112] the non-linear model of the MOD-2 wind turbine is developed. The parameters chosen for the wind turbine are tabulated in Table 5.2.

Table 5.1: PMSG PARAMETERS

PARAMETER	VALUE
Per phase inductance(L_s)	0.0036 H
Stator Resistance (R_S)	0.6 Ω
Rated power	5 kW
Voltage constant	300 V/krpm

Table 5.2: WIND TURBINE PARAMETERS

PARAMETERS	VALUE
Blade pitch (β)	0°
Blade Radius(r)	80 cm
Air density (ρ)	1.225 kg/m^3
Nominal Lambda(λ_n)	8.035
C_p at λ_n	0.475

5.3.2 SCIM control

A 5 KW, 2 pole SCIM is selected to be emulated as the wind turbine. The controls are implemented using CP1104 dSPACE. Using the turbine model given in section 5.3.1 a Matlab model is developed, which generates the reference torque for the SCIM.

The stator and rotor Leakage Inductance(L_s and L_r), Mutual Inductance (L_m), steady state flux (ψ), stator and rotor resistance(R_s and R_r) are calculated by performing no-load and block-rotor tests on the SCIM. The FOC is implemented on the SCIM as follows:

- The stator currents(I_a, I_b, I_c) are measured and converted to the d-q reference frame(I_d, I_q) using park transformation.

- The I_q is used to calculate the value of slip speed in the SCIM using,

$$\omega_s = \frac{L_m I_q}{\tau \psi_r} \tag{5.17}$$

$$\text{Where,} \qquad \tau = \frac{L_m + L_r}{R_r} \tag{5.18}$$

This calculated slip is added to the measured rotor speed of the machine to get the

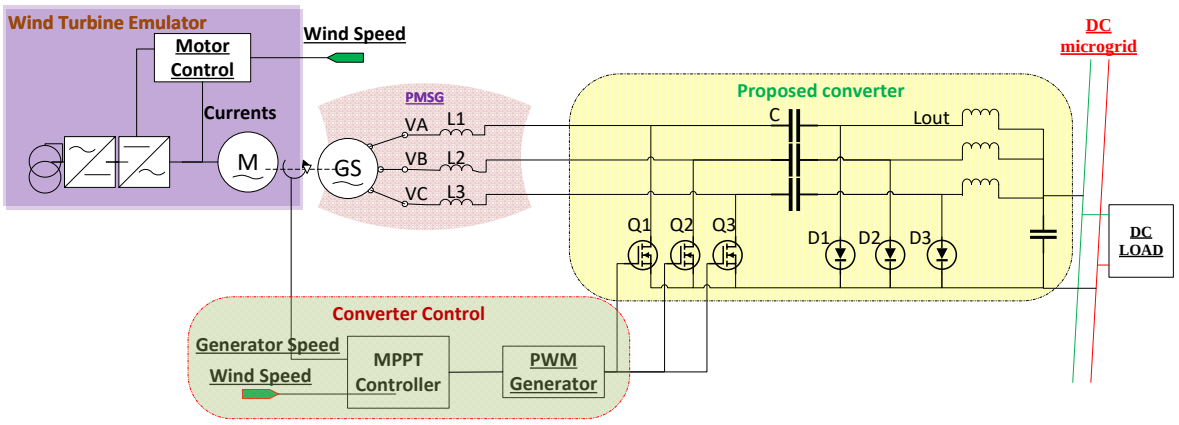

Figure 5.7: The schematic diagram of wind energy emulation and conversion system.

electrical angle of stator currents needed to get the desired torque value.

$$\omega_e = \omega_r + \omega_s$$

By using the measured value of I_d the value rotor flux in (5.17) can be estimated by:

$$\psi_r = (\frac{L_m}{1+\tau s})i_d$$

To be implemented using digital system the laplace transform is changed to z-domain, putting in the values given in Table 5.3

$$\psi_r = \frac{0.0001023z + 0.0001023}{z - 0.9996}$$

The Torque of the machine is needed to be estimated accurately in order to implement the torque control for turbine emulation, the torque is estimated by:

$$T_e = \frac{3}{2}P\frac{L_m}{L_m + L_r}(\psi_r i_q) \tag{5.19}$$

Here, P is the number of pole pairs in the SCIM; thus, P=1.

The values of the different motor parameters used in (5.17)(5.18)(5.19) is collated in Table 5.3. The values of the I_d and I_q are DC in nature; thus, PI controllers are deemed sufficient to control the stator currents by generating voltage reference for the VSI. The Torque reference is generated by using (16), and the flux reference is set at a value calculated by doing the no-load test on the SCIM. In this work, the reference value of flux is set at 0.76241 webers. A PI controller having proportional gain (K_p) of 0.1 and Integral gain(K_i) of 2 is used for both the torque and flux controllers.

Table 5.3: MOTOR PARAMETERS

PARAMETER	VALUE
Stator Leakage Inductance(L_s)	0.0103 H
Rotor Leakage Inductance(L_r)	0.0103 H
Stator Resistance (R_S)	2.47 Ω
Rotor Resistance(R_r)	2.0845 Ω
Mutual Inductance(L_m)	0.5498 H
Motor time constant (τ)	0.2687 s

5.3.3 Converter design

The converter design is done to keep the input inductor in CICM and the input impedance of the three-phase circuit maximum at the power line frequency. The design parameters assumed for this work are given in Table 5.4. As the converter is intended to be placed near the wind turbine, the noise produced at audible frequency is not considered. Thus the working frequency of 10 kHz is selected. The advantage of direct coupling of PMSG to the turbine is the elimination of gearbox and consequent decrease in cost, but the commercially available PMSGs have a low voltage constant. A 6-pole PMSG is used in this work; thus, for better power extraction from the generator, the converter is designed to work at a low input RMS voltage.

It is convenient to do the calculations in the per phase quantities, the design methodology is as follows:

* Max input voltage per phase $V_m = \sqrt{2}V_{in}$

- Maximum operating Duty(D_{max}) for DICM operation of output inductors is taken as 70 %.

- The per phase load (R) of converter is $(3V_o^2/P_o)$ Ω.

The value of the input inductor is taken as the per phase inductance of the PMSG; thus, $L_1 = L_s$.

The critical value of K_a is calculated as:

$$K_a(critical) = \frac{1}{2(1+M)^2} = \frac{1}{2(1+V_o/V_m)^2} \tag{5.20}$$

The value of equivalent inductance(L_{eq}) is calculated as:

$$\frac{1}{L_{eq}} = \frac{1}{L_1} + \frac{1}{L_{11}} \tag{5.21}$$

$$L_{eq} = \frac{RK_aT_s}{2} \tag{5.22}$$

For $L_1 >> L_{eq}$ and using (22) and (23),

$$L_{11} = \frac{L_1 L_{eq}}{L_1 - L_{eq}} \approx L_{eq} \tag{5.23}$$

The value of capacitor C_1 is chosen such that its resonant frequency with L_1 lies near the logarithmic mean of power frequency and switching frequency. C_1 also decides the input impedance of the converter at power frequency. Thus its value is chosen to keep the input impedance high in order to reduce the circulating current.

The value of the DC link capacitor is selected in order to get minimum voltage ripple at rated output power, the value of output capacitor is chosen to be 1000 μF. At this value, the voltage ripple is found to be less than 2 % even in standalone operation without DC microgrid.

Table 5.4: DESIGN PARAMETERS

PARAMETER	VALUE
Input rms Voltage(V_{in})	100 V
Output Power(P_o)	1000 W
Output Voltage(V_o)	230 V
Operating Frequency (f)	$10KHz$
Input inductance (L_1)	3.6 mH

Table 5.4 recapitulates the design parameters selected for this work and Table 5.5 states the calculated and selected values of the converter parameters.

5.3.4 MPPT and system description

The maximum power extracted from an ideal wind turbine is only 59.26 % of the input wind power. In the field, less than 50 % efficiency is achieved at best. It makes the use of an MPPT system pivotal in WECS. For fixed blade pitch turbines used in small-scale wind generation, TSR's value decides the value of C_p; thus, the TSR-MPPT technique

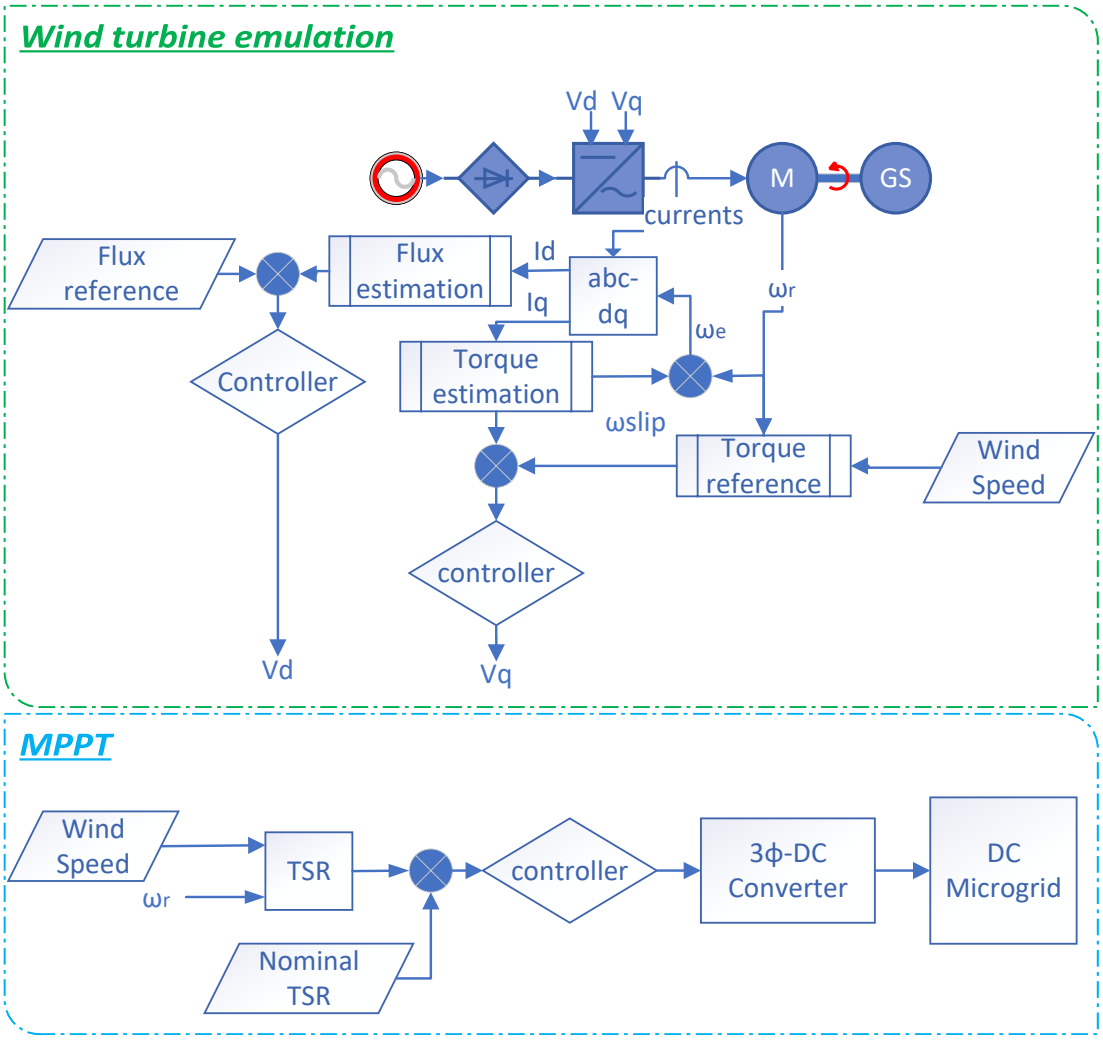

Figure 5.8: System description for wind turbine emulation.

Table 5.5: CONVERTER PARAMETERS

CONVERTER PARAMETER	VALUE
$K_a \leq K_a(critical)$	0.07
Equivalent inductance (L_{eq})	555 μH
Output Inductor(L_{11})	560 μH
Capacitor(C_1)	1 μF
DC link Capacitor (C_o)	1000 μF

is used in this work. A change in wind speed results in a change in the value of TSR (λ), which results in a change in the duty cycle of the converter. The duty cycle of the converter adjusts the power extracted from the PMSG and hence leads to a change in torque and speed of the wind turbine. Thus, by employing a PI controller to match the value of TSR to the nominal TSR value, MPPT is achieved.

The schematic diagram of the system is given in Figure 5.7. The motor control is described in Figure 5.8. The MPPT technique is simple to implement using a PI controller with saturation at 0 to 0.7. The PI controller has back-calculation as the anti-windup method. The value of K_p and K_i used for TSR-MPPT control are 0.2 and 5, respectively. For a MOD-2 turbine, emulated in this work, the optimum TSR value at 0° blade pitch is found to be 8.035. The corresponding value of C_p to the selected value of nominal TSR is found to be 47.5 %, which is the highest value at all wind speeds.

5.4 Simulation Results

The system represented in Figure 5.7 is simulated in Matlab/Simulink version 8.9, with variable step and ode23tb solver. The calculations for flux estimation, torque reference generation, and PI controller are done at a fixed step time of 0.0001 seconds.

The simulation result of the converter showing the input waveform of three-phase voltages across switches and input currents is given in Figure 5.9. The simulated result shows the inherent PFC at converter input due to the DICM operation of the output inductors. As the star point of the generator is not available for measuring the phase voltages, the common source point in the converter is taken as a pseudo star point for measuring the phase voltage, which is effectively the voltage across the switches. Al-

though, the switching voltage stress is in phase with the per phase voltage. The input inductors are inside the PMSG and are working in CICM. Thus, the measured voltage at any instance of time is not equal to the phase voltage.

Figure 5.11 shows the maximum voltage stress across the diode and switch of phase R. The DICM operation of the output inductor leads to reduced average voltage stress across the switch and a lower conduction period of the diode. When the output inductor current becomes zero, the voltage stress across the switch becomes (intermediate phase capacitor - DC microgrid voltage).

Figure 5.12 presents a zoomed view of the states of the converter at the maxima of the input current in phase R. The waveform of the input inductor current, output inductor current, and the voltage of the intermediate capacitor is shown during the switching.

The efficiency of the three-phase AC to DC conversion system used in [116] for WECS is compared with the proposed converter. The efficiency curve with change in converter duty cycle is given in Figure 5.13. The efficiency of the uncontrolled DBR is also shown, and it can be observed that the efficiency of the proposed converter attains similar values as the DBR in the duty range of around 35 percent.

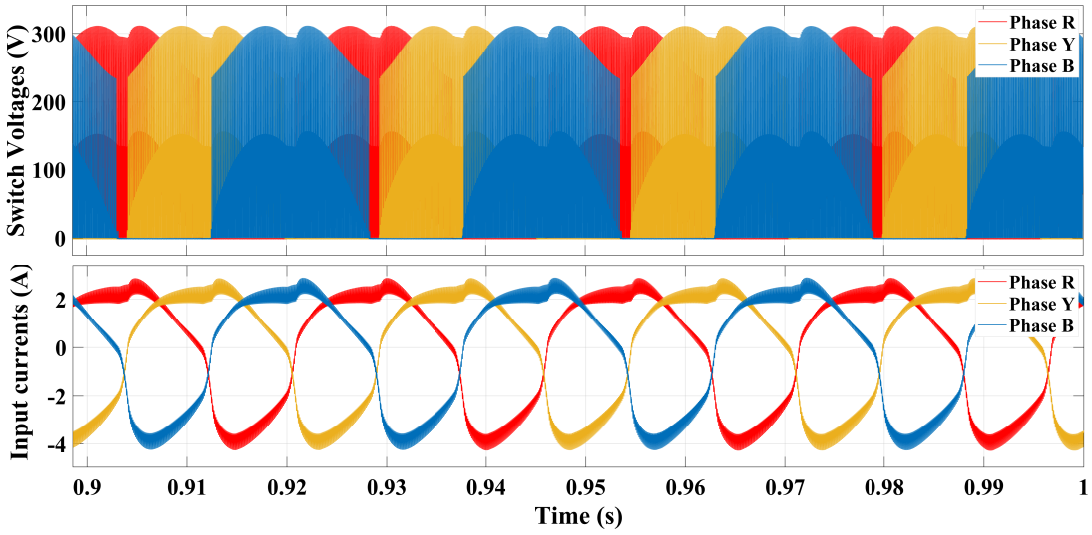

Figure 5.9: Voltage across switches and input current.

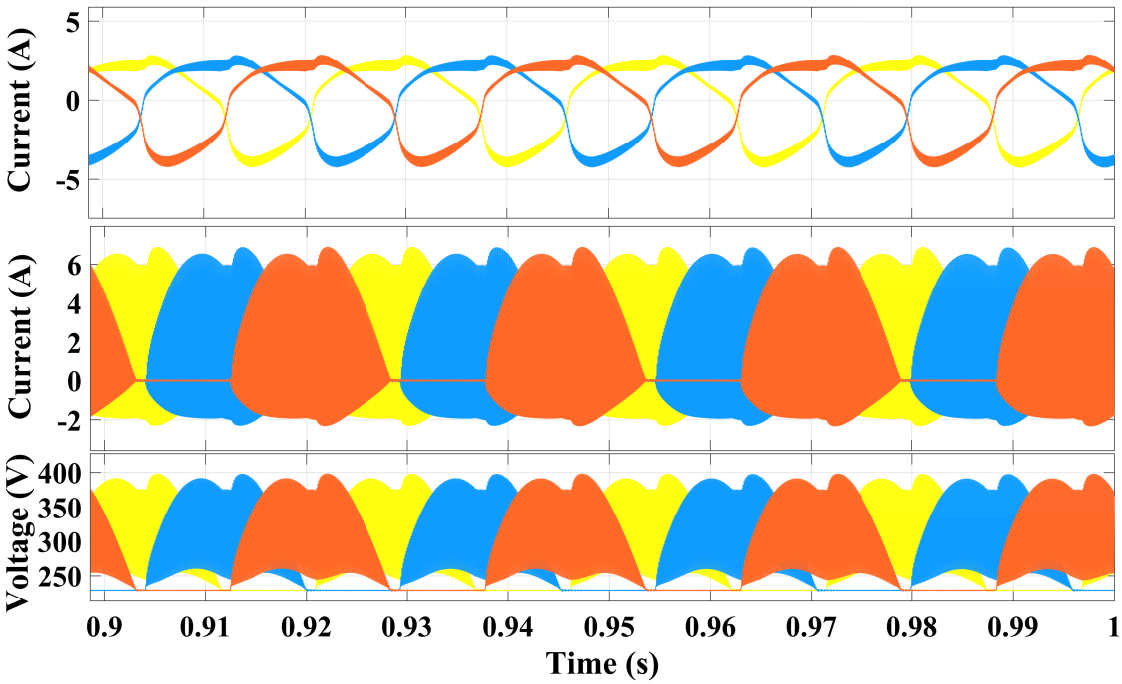

Figure 5.10: Input current, output current and capacitor voltages.

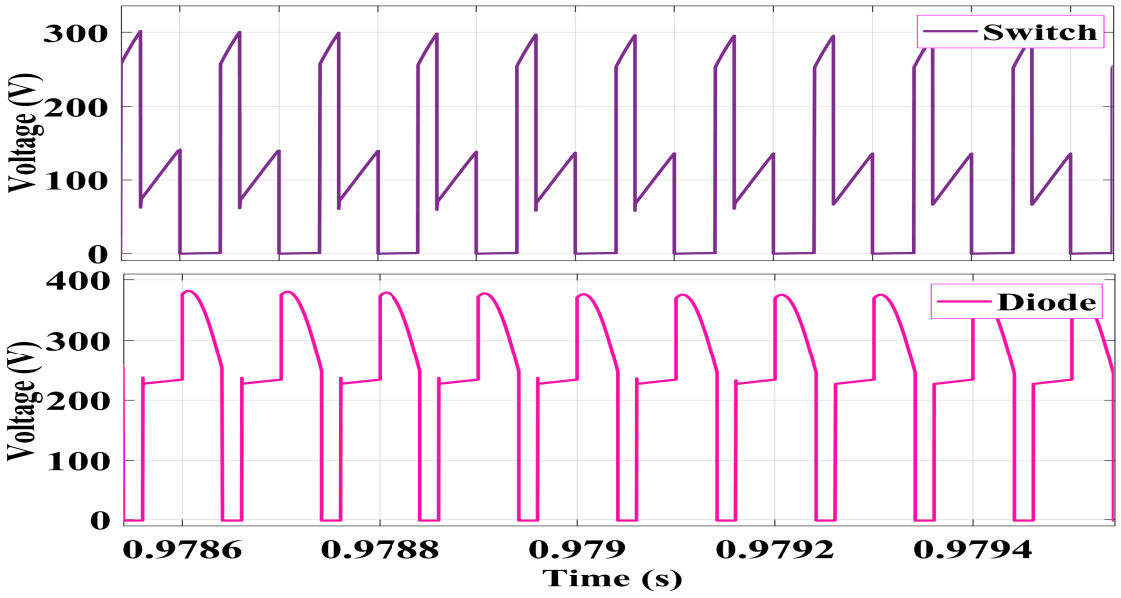

Figure 5.11: Voltage stress across diode and switch of phase R.

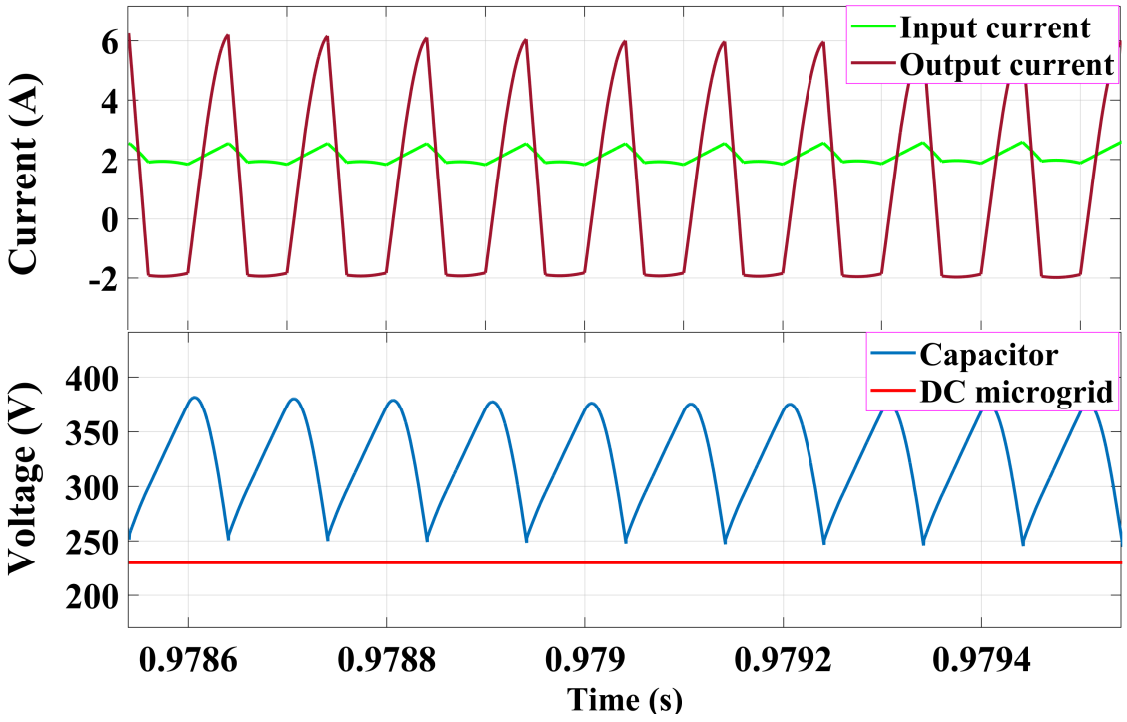

Figure 5.12: Input current, output currents and capacitor voltage of phase R.

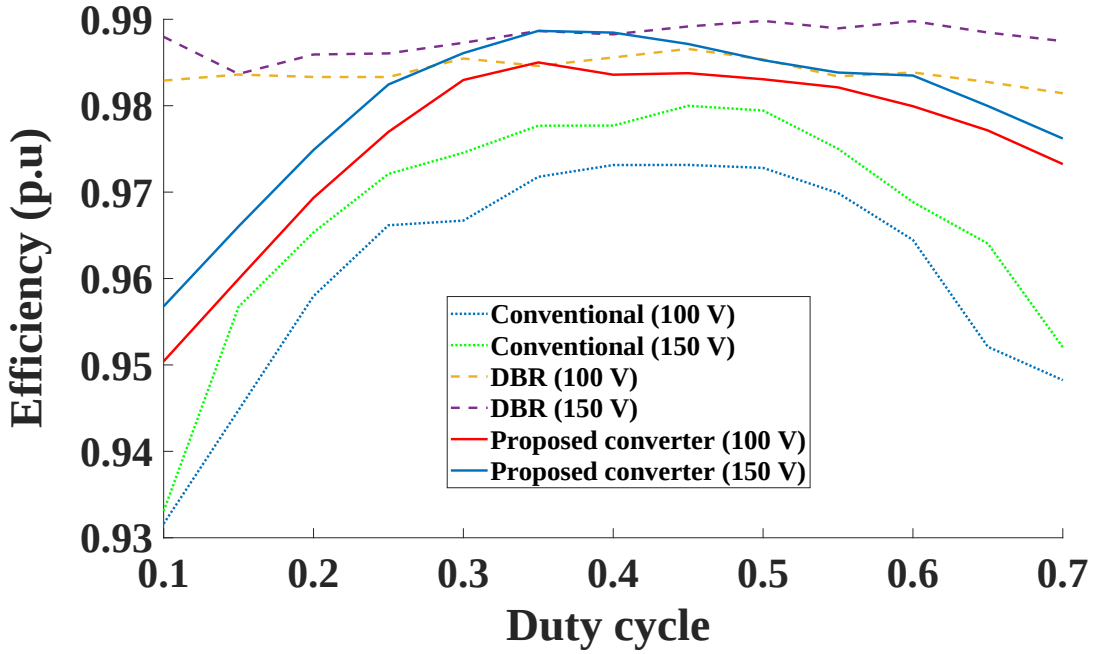

Figure 5.13: Comparative efficiency plot of proposed converter with DBR and conventional converter.

5.5 Hardware Results

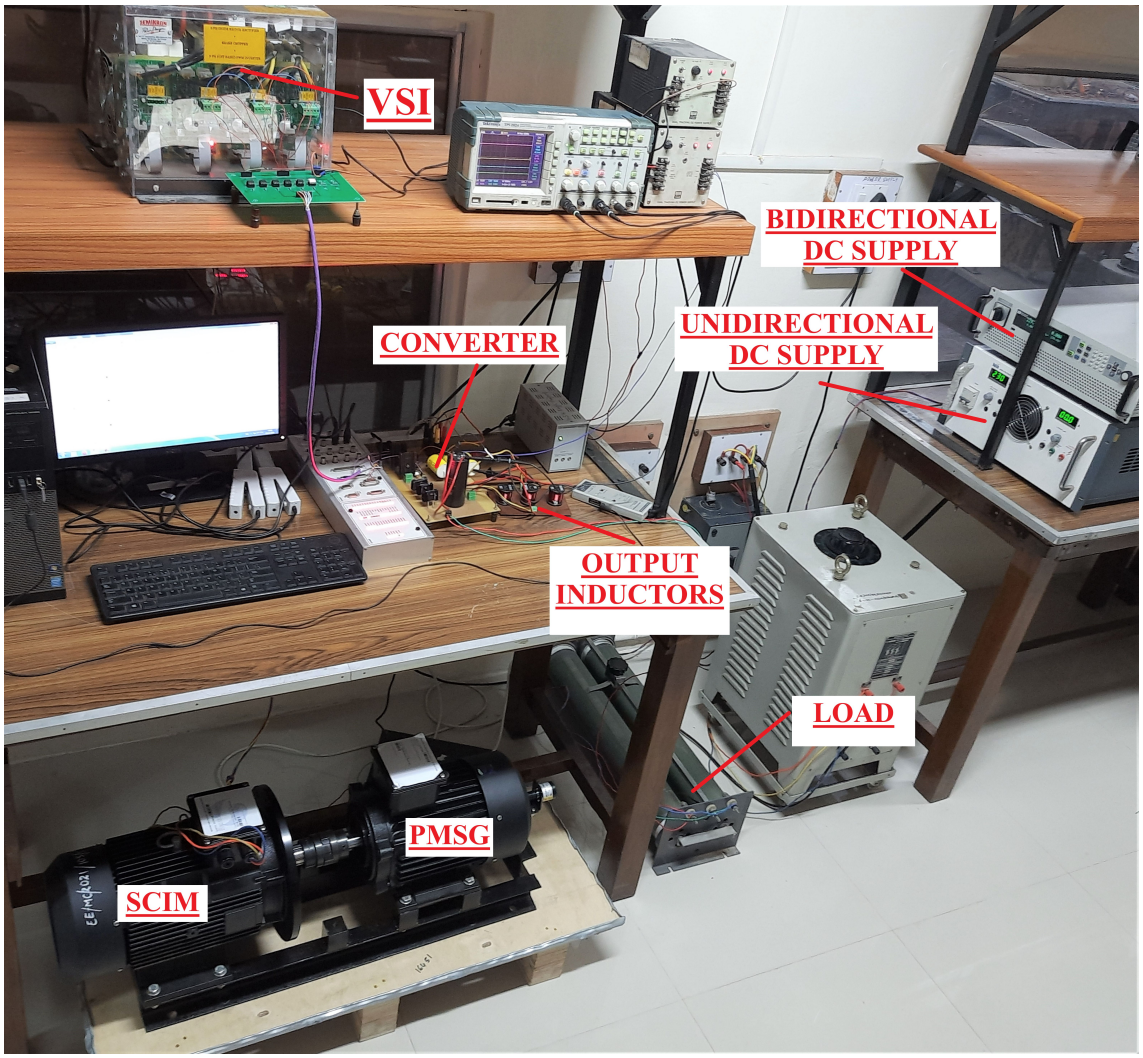

Figure 5.14: Laboratory setup.

The developed converter is tested with a PMSG driven by a wind turbine emulator. The wind turbine emulator is developed using a three-phase 5.5 KW induction motor. The components used in developing the converter are given in Table 5.6. The input inductor value is 3.6 mH, which is the per-phase inductance of the PMSG used in this work. The output inductors of 560 μH as per the designing done in section 5.3.3 is used. The controlling of the emulator and the converter is done using CP1104 d-SPACE. Figure 5.14 shows the laboratory setup for the wind turbine emulation and the PMSG based WECS.

The three-phase input currents are shown in Figure 5.15. It is observed that the waveform of the currents is similar to the current waveform of a three-phase brushless DC motor (BLDCM). A dip in current is observed at the maxima of each cycle due to phase

Table 5.6: COMPONENT DESCRIPTION

Component	part number	quantity
Inductors	PCV-2-564-08L	3
Capacitor 1μF	MKP C.4C	3
Capacitor 1 mF	ALC70C 102 FP	1
IGBTs	K40H1203	3
Diodes	DSEI60-10A	3

change. A PMSG with trapezoidal back-emf is used in this work due to its high voltage gain.

Figure 5.16 shows the three-phase output inductor currents. The DCIM operation of the output inductors is evident from the shown results at all voltage levels. The dip in current at the maxima of the input inductor current is also reflected in the output inductor currents. It is also observed that the output inductor currents become negative by the same value as the positive current in input inductors, which allows a higher value of current ripple without saturation of the inductors.

Figure 5.17 shows the phase shift between the input current and output current with the voltage stress on the switch of phase-R. There is no phase shift between the input and output inductor currents due to DICM operation. Also, as the input inductors are inside the PMSG, the switching stress is the only available measurement equivalent to the input phase voltage. It can also be observed that the switching stress on the switch is zero in the negative half cycle.

The zoomed view of the input inductor current, output inductor current, and the switching stress in switch of phase-R at the maxima of input inductor current are shown in Figure 5.18. The voltage stress on the diode of phase-R under the same operating condition is shown in Figure 5.19. The obtained waveforms are similar to the simulated results shown in Figure 5.11. The explanation for the stress profiles is given in section IV. A ringing in the voltage stress due to parasitic components of the switch and diode is observed when the current of the output inductor becomes zero.

All the states of the converter, i.e., input current, output inductor current, and intermediate capacitor voltage, is shown in Figure 5.20 at the maxima of the input current

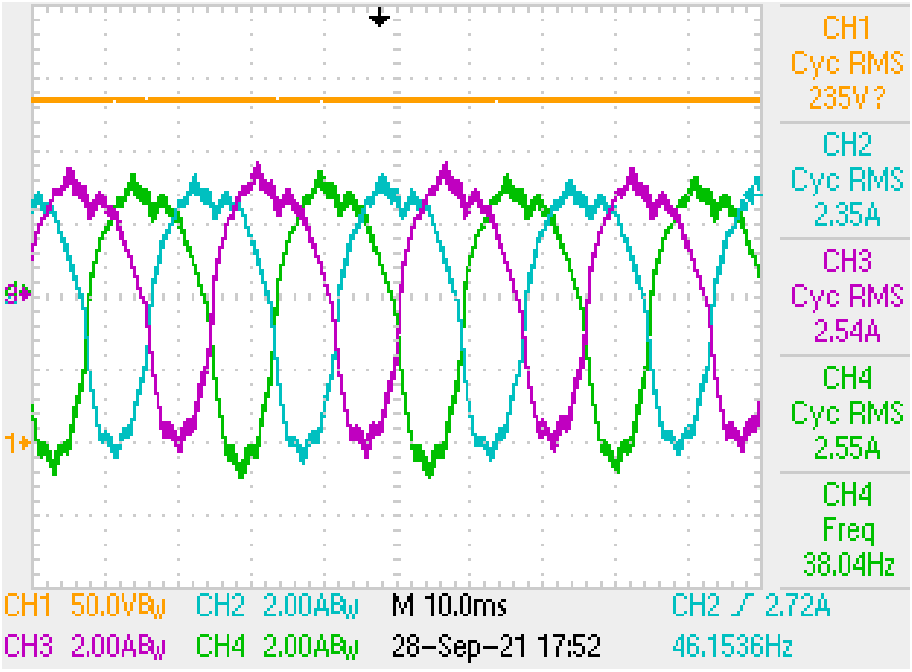

Figure 5.15: Voltage of DC microgrid (channel-1) and three-phase input current (channel-2,3,4).

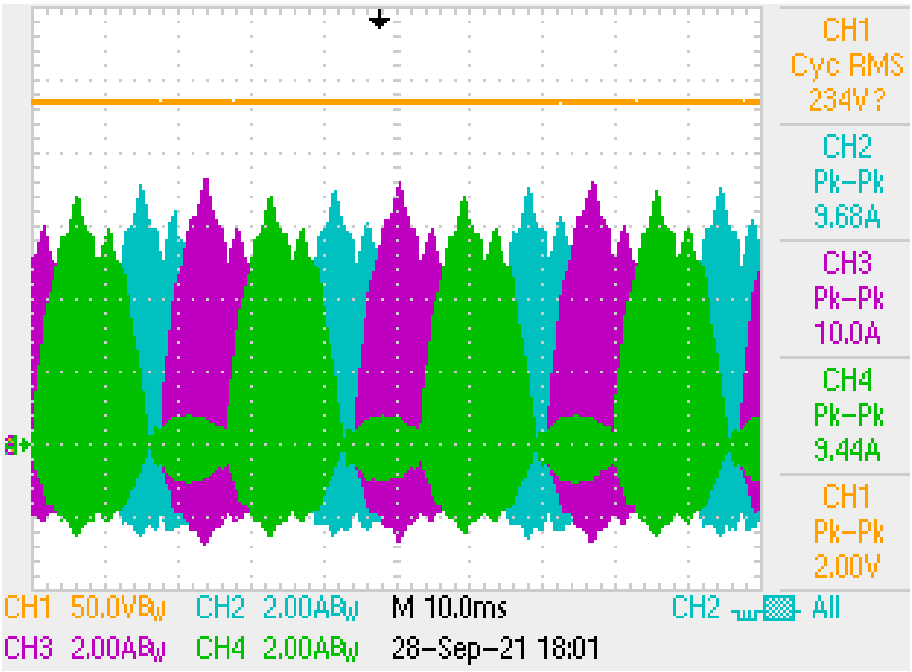

Figure 5.16: Voltage of DC microgrid (channel-1), three-phase output inductor currents (channel-2,3,4).

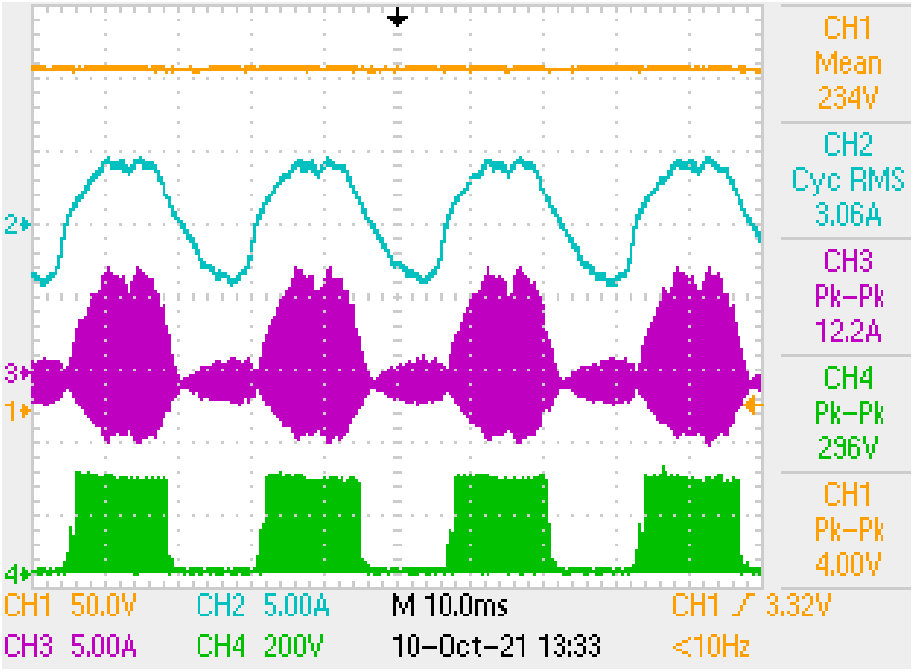

Figure 5.17: DC microgrid voltage (channel-1), input inductor current of phase-R (channel-2), output inductor current of phase-R (channal-3), voltage stress on switch of phase R (channel-4).

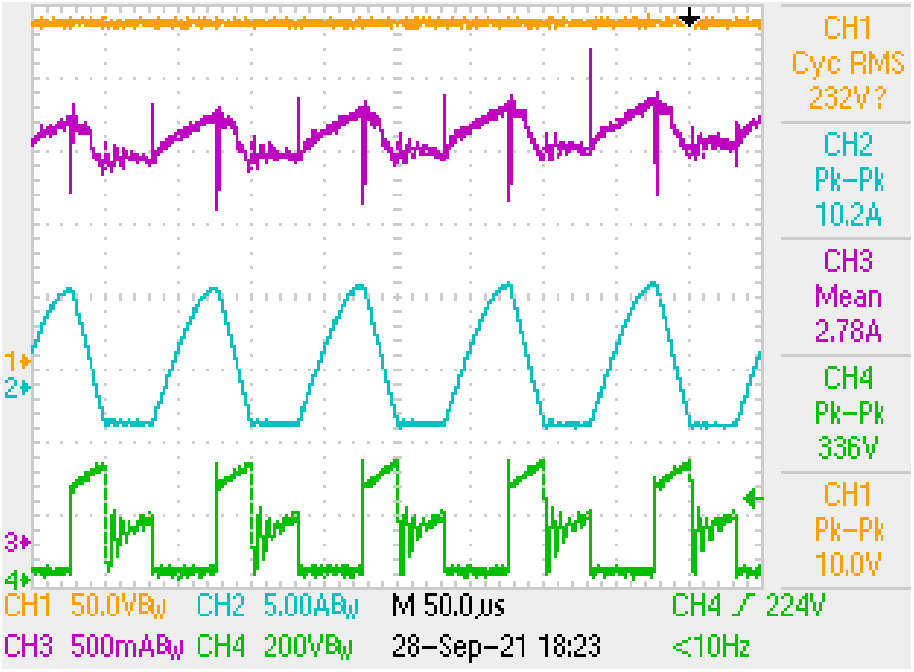

Figure 5.18: Zoomed view of the output inductor current (channel-2), input inductor current (channel-3), and voltage stress on switch (channel-4), DC microgrid (channel-1).

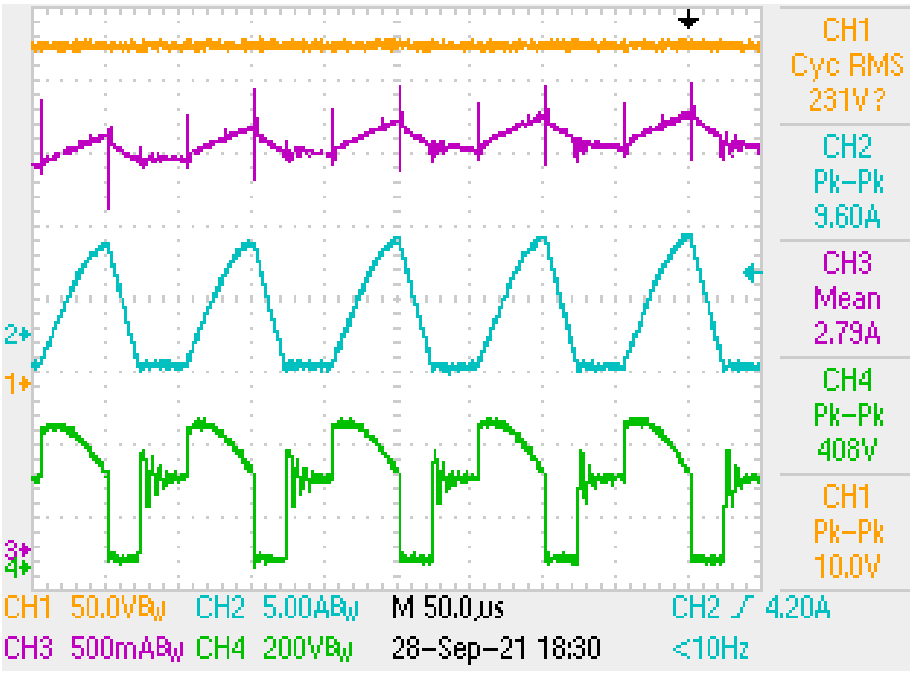

Figure 5.19: Zoomed view of the output inductor current (channel-2), input inductor current (channel-3), and voltage stress on diode (channel-4), DC microgrid (channel-1).

of phase R. The waveform are similar to the simulated results shown in Figure 5.12. The developed WECS is tested for wind speed variation from 5 m/s to 12 m/s. The input power is measured as the product of estimated torque and the measured rotor speed. The output power is measured as the product of microgrid voltage and the total output current of the converter. The measured input power, rotor speed, and conversion efficiency are tabulated in Table 5.7 with variation in wind speed.

Table 5.7: SYSTEM PERFORMANCE

WIND (m/s)	ROTOR (rpm)	POWER (W)	EFFICIENCY(p.u)
5	480	73	0.849
5.5	526	97.5	0.8666
6	580	126.8	0.8832
6.5	620	161	0.8913
7	680	201	0.905
7.5	720	247	0.894
8	770	300	0.883
8.5	820	360	0.9
9	860	427	0.92
9.5	910	500	0.931
10	980	590	0.921
10.5	1010	680	0.912
11	1050	780	0.897
11.5	1100	880	0.891
12	1150	1015	0.906

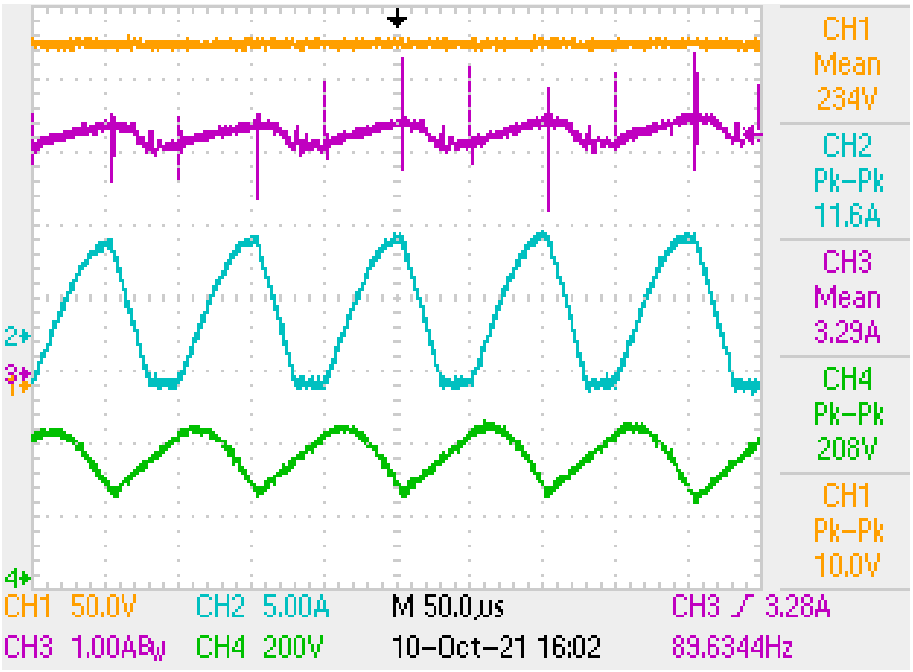

Figure 5.20: Voltage of microgrid (channel-1), output inductor current (channel-2), input inductor current (channel-3), capacitor voltage (channel-4).

5.6 Summary

A PMSG based WECS using a new three-phase AC to DC converter is designed, analyzed, and tested in this chapter. The developed energy conversion system and the TSR-MPPT employed in this work are found to be working satisfactorily during experimental validation at different wind speeds in a 230 V DC microgrid. The elimination of front-end DBR, gearbox, and input inductors make the developed converter highly compatible with PMSG. The result obtained from simulations and the laboratory prototype consolidates the frugality of using this system in WECSs feeding a DC microgrid.

After mitigating the limitations of the converters in the photovoltaic and wind power generation systems, the next chapter deals with development of a photovoltaic-wind hybrid energy conversion system(HECS).